Surface silane-functionalized Fe_2O_3 nanoparticles for dual pickering emulsion stabilization and fenton-Type catalytic oxidation

Nanopartículas de Fe_2O_3 funcionalizadas superficialmente con silano para la estabilización dual de emulsiones pickering y oxidación catalítica tipo Fenton

W. G. Oyola Naranjo ; V. G. Baldovino-Medrano ; F. M. Ortega

DOI: https://doi.org/10.22517/23447214.26487
Scientific and technological research paper

***Abstract*— Enhanced thermal recovery of heavy crude oils requires multifunctional nanomaterials capable of stabilizing interfaces and catalyzing oxidation reactions under reservoir conditions. Fe_2O_3 nanoparticles (Fe_2O_3-NPs) are promising candidates due to their redox activity and potential as Pickering emulsion stabilizers, although their dual performance depends on precise control of surface chemistry. The objective was to design and characterize dual-function Fe_2O_3-NPs, active as Pickering emulsion stabilizers and Fenton-type catalysts, through controlled surface functionalization with silane coupling agents (SiCAs). Fe_2O_3-NPs were functionalized with propyltrimethoxysilane (C3), octyltriethoxysilane (C8), and hexadecyltrimethoxysilane (C16) via hydrolysis of alkoxy groups and condensation with surface –OH groups, characterizing BET surface area, particle size (DLS), contact angle, and surface chemistry (XPS, FTIR-ATR); the nanoparticles were used to formulate polar and nonpolar nanofluids, evaluating their interfacial activity in water/hydrocarbon Pickering emulsions at different particle loadings. Functionalization modulated interfacial activity, with contact angles ranging from 20° to 167°, without significant loss of active surface area or multilayer formation; emulsion stability and type (O/W or W/O) correlated with the particles' hydrophilic–hydrophobic balance. Fe_2O_3 active sites were preserved after functionalization, enabling dual performance as an interfacial stabilizer and heterogeneous oxidation catalyst, with potential application in in-situ combustion processes for thermal recovery. This work was funded by Colciencias-ANH, project "Preparation of transition metal-based nanomaterials for processes related to thermal recovery of Colombian crude oils and analysis of their catalytic behavior in in-situ combustion processes."**

***Index Terms*—Catalytic oxidation; Fe_2O_3 nanoparticles; Pickering emulsions; Silane coupling agents; Surface functionalization.**

***Resumen*— La recuperación térmica mejorada de crudos pesados requiere nanomateriales multifuncionales capaces de estabilizar interfases y catalizar oxidaciones en condiciones de yacimiento. Las nanopartículas de Fe_2O_3 (Fe_2O_3-NPs) son candidatas prometedoras por su actividad redox y potencial como estabilizadores de emulsiones Pickering, aunque su desempeño dual depende del control de la química superficial. El objetivo fue diseñar y caracterizar Fe_2O_3-NPs de doble función, activas como estabilizadores de emulsiones Pickering y catalizadores tipo Fenton, mediante funcionalización superficial con agentes de acoplamiento de silano (SiCAs). Las Fe_2O_3-NPs se funcionalizaron con propiltrimetoxisilano (C3), octiltrietoxisilano (C8) y hexadeciltrimetoxisilano (C16) mediante hidrólisis de grupos alcoxi y condensación con grupos –OH superficiales, caracterizando área BET, tamaño de partícula (DLS), ángulo de contacto y química superficial (XPS, FTIR-ATR); las nanopartículas se emplearon en nanofluidos polares y no polares, evaluando su actividad interfacial en emulsiones Pickering agua/hidrocarburo a distintas concentraciones. La funcionalización moduló la actividad interfacial, con ángulos de contacto entre 20° y 167°, sin pérdida de área activa ni formación de multicapas; la estabilidad y el tipo de emulsión (O/W o W/O) se correlacionaron con el balance hidrófilo-hidrófobo de las partículas. Los sitios activos de Fe_2O_3 se conservaron tras la funcionalización, permitiendo desempeño dual como estabilizador interfacial y catalizador de oxidación heterogénea, con potencial aplicación en combustión in-situ para recobro térmico. Este trabajo fue financiado por Colciencias-ANH, proyecto "Preparación de nanomateriales basados en metales de transición para procesos ligados al recobro térmico de crudos colombianos y análisis de su comportamiento catalítico en procesos de combustión in-situ"**

***Palabras claves*— Agentes de acoplamiento de silano; Emulsiones Pickering; Funcionalización superficial; Nanopartículas de Fe_2O_3; Oxidación catalítica.**

I. INTRODUCTION

THE Fe_2O_3-NPs are valued as catalysts because they combine redox flexibility, surface oxygen mobility, visible-light activity, chemical stability, magnetic recoverability, and easy surface functionalization.[1], [2].

This manuscript was submitted on August 6, 2026, accepted on September 8, 2026, and published on September 30, 2026. This work was supported by School of Chemistry of the Industrial University of Santander and Catalysis Research Center.

Wilson Oyola has a master's degree in chemistry and is a PhD candidate in chemistry at the Industrial University of Santander, Colombia, wilson2148230@correo.uis.edu.co.

Victor G. Baldovino is an Associate Professor at the School of Chemical Engineering, leadership position as Director of and Catalysis Research Center and Surface Science Laboratory, vicbaldo@uis.edu.co.

Fernando Martinez is an Associate Professor at the School of Chemistry of the Industrial University of Santander, and he is part of the Catalysis Research Center, Guatiguará Technology Park Km 2 via Refugio, Piedecuesta, Santander, Colombia., fmartine@uis.edu.co

CC BY NC SA

These properties make them versatile for oxidation reactions, environmental catalysis, photocatalysis, and functional interfaces such as emulsions. Particularly, Fe_2O_3 (including α-Fe_2O_3 and γ- Fe_2O_3) nanoparticles and their composites have gained significant attention in recent years due to their unique properties and versatile applications.[3], [4], [5], [6],[7], [8].

Their catalytic efficiency can be enhanced by controlling the particle size, shape, and surface modifications.[9] In addition. Fe_2O_3-NPs have been shown to catalyze the degradation of methylene blue, significantly improving the efficiency of the Fenton reaction. Moreover, they are used in the supercritical upgrading of heavy petroleum oils, showcasing their potential in the energy sector.[10] Their ability to undergo phase transitions while maintaining structural integrity further enhances their catalytic performance.[11] The magnetic properties of these nanoparticles also facilitate their recovery and reuse, making them cost-effective catalysts.[9], [12] In aqueous environments, Fe_2O_3 can activate free radical generation through advanced oxidation processes, producing highly reactive hydroxyl radicals (OH·) in what is known as the Fenton process. [9], [10], [13]

Surface modification with silane coupling agents (SiCA) has proven effective for functionalizing oxide nanoparticles due to their ability to form strong covalent bonds between organic and inorganic materials.[14], [15], [16], [17] A covalent bond formation between the tri-alkoxy group and the free -OH groups on the oxide nanoparticle surface, creating a dynamic interfacial chemistry that generate tunable heterogeneous environments with tailored properties.[16], [17], [18]

Fe_2O_3-NPs exhibit distinctive behavior as Pickering stabilizers due to their intermediate wettability, pH-responsive surface charge, and abundant surface hydroxyl groups, which promote strong and often irreversible adsorption at the oil–water interface.[19], [20] TiO2 particles also stabilize O/W emulsions effectively and offer additional photocatalytic functionality under UV irradiation, although their interfacial behavior is less tunable than that of Fe_2O_3.[21] Beyond their stabilizing role, Fe_2O_3-NPs provide unique advantages, including intrinsic redox activity (Fe^{3+}/ Fe^{2+} cycling) and magnetic responsiveness, enabling dual-function systems where the same particles act simultaneously as interfacial stabilizers and heterogeneous catalysts. The coupling of Pickering emulsion stabilization with heterogeneous catalytic oxidation has been demonstrated with fluorinated silica particles bearing Pd nanoparticles, which achieved up to 7–10 times higher activity for aerobic benzyl alcohol oxidation in oil foams compared to conventional non-foam systems.[22], [23]

In this work, we investigate the surface functionalization of Fe_2O_3-NPs using three silane coupling agents differentiated by the length of the organic chain attached to the silicon atom. Particularly, we examine the impact of these modifications on particle hydrophilicity modulation to select suitable functional agents for broad-spectrum surface modification and emulsion stabilization without completely covering the active surface, the formulation of emulsion and nanofluids, thus maintaining catalytic activity for benzyl alcohol oxidation via a Fenton-type mechanism.

II. Methodology

A. *Synthesis of Fe_2O_3-NPs*

Materials

Iron chloride (III) ($FeCl_3.6H_2O$, >98%), sodium carbonate (Na_2CO_3, >98%), propyltrimethoxysilane (PTMS, C3), octyltriethoxysilane (OTES, C8), and hexadecyltrimethoxysilane (HDTMS, C16) were purchased from Sigma-Aldrich. Ethanol, toluene, and n-heptane were obtained from Merck. All chemicals were used as received without further purification.

Synthesis protocol

The synthesis procedure was carried out using a stirred reactor with temperature control and an addition funnel for the sodium carbonate solution. Fe_2O_3-NPs were prepared via an alkaline coprecipitation method following established protocols with modifications.[24] Briefly, ~1.0000 g of $FeCl_3$ was weighed and transferred to a 250 mL glass beaker. Acetone (50 mL, HPLC grade) was then added, and the mixture was stirred using a magnetic stirrer at 500 rpm for 15 min at room temperature until complete dissolution. Separately, Na_2CO_3 (1.0000 g) was transferred to a 250 mL beaker, ultrapure water was added, and the mixture was stirred magnetically at 400 rpm for 10 min until complete dissolution was achieved, yielding a clear solution.

The Na_2CO_3 aqueous solution was added dropwise to the $FeCl_3$/acetone solution using a burette under vigorous magnetic stirring (800 rpm) at room temperature. The mixture was continuously stirred for 30 min during the addition and for an additional 30 min after complete addition. Throughout this process, vigorous CO_2 gas evolution was observed, and the formation of a brown precipitate was obtained.

The resulting precipitate was recovery by centrifugation (3000 rpm, 10 min) and the supernatant was carefully decanted. This washing procedure was repeated three times.

Subsequently, the precipitate was washed twice with pure acetone to remove residual water, followed by two washes with dichloromethane to facilitate complete water removal. The washed precipitate was transferred to a ceramic crucible and dried at 60°C for 1 hour in an oven (Thermo Scientific Thermolyne, USA) to evaporate residual dichloromethane. Finally, the dried sample was transferred to a ceramic crucible placed in the central zone of the oven and dried at 200°C for 3 h (heating rate: 5°C/min, air atmosphere).[25]

B. Physicochemical properties of the synthesized Fe2O3-NPs

Particle size distribution

Particle size distribution was measured using a Litesizer 500 instrument (Anton Paar, Austria) equipped with a 658 nm laser diode operating in backscatter mode at 175° (NIBS technology). Dried nanoparticle samples (5.0 mg) were dispersed in ultrapure water (Type I, 10 mL) to a concentration of 500 ppm, sonicated for 5 minutes at room temperature, and transferred to disposable polystyrene cuvettes.

Porosity and specific surface area

Specific surface area and pore size distribution measurements were estimated using a 3Flex Surface Characterization Analyzer (Micromeritics Instrument Corporation, USA). About 150-200 mg of samples were accurately weighed and transferred to glass analysis tubes (9 mm outer diameter). Fe2O3 and functionalized samples were degassed in a SmartVacPrep degassing station (Micromeritics) at 120°C for 12 h under high vacuum (<10 μmHg) to remove adsorbed moisture and volatile contaminants. After degassing, the tubes were backfilled with nitrogen gas, sealed, and the exact sample mass was recorded. N2 adsorption-desorption isotherms were measured at 77 K.[26]

The adsorption isotherm was collected over a relative pressure (P/P_0) range of 0.005 to 0.995. The desorption branch was measured from P/P_0 = 0.995 to approximately 0.10 to determine pore size distribution and detect hysteresis effects. Data analysis was performed using the 3Flex software. The specific surface area was calculated using the Brunauer-Emmett-Teller (BET).

Crystallinity

The crystallinity and phase composition of the synthesized Fe_2O_3-NPs were evaluated by X-ray diffraction (XRD) using a BRUKER D8 ADVANCE powder diffractometer (Bruker AXS, Germany) equipped with DaVinci geometry. The instrument was operated at 40 kV and 40 mA using a Cu sealed tube as the X-ray source, providing Cu Kα radiation (λ = 1.5406 Å). For sample preparation, finely ground powder samples (~50-100 mg) were homogenized in an agate mortar and reduced to a particle size of less than 38 μm (400 mesh), then mounted on polymethyl methacrylate (PMMA) supports using the front-filling technique. Diffraction patterns were recorded over a 2θ range of 10° to 70° with a step size of 0.02°. Phase identification was conducted by comparing experimental patterns with reference patterns from ICDD database. Crystallite size was estimated using the Scherrer equation: $D = K\lambda/(\beta \cos\theta)$, where K=0,9 (spherical particles), λ =1.54056 Å, β is the FWHM corrected for instrumental broadening, and θ is the Bragg angle.[27]

Analyze IR of Fe2O3 and functionalized Fe_2O_3-NP samples

The functional groups of the synthesized materials were analyzed by Fourier transform infrared (FTIR) spectroscopy using a Nicolet iS50 FT-IR spectrometer (Thermo Fisher Scientific, USA) in attenuated total reflectance (ATR) mode with a single-reflection diamond crystal accessory.

Dry powder Fe_2O_3 and functionalized Fe_2O_3-NP samples (~2–5 mg) were placed onto the diamond crystal and pressed uniformly to ensure intimate contact. Spectra were acquired over 400–4000 cm-1 with 4 cm-1 resolution by co-adding 32 scans. At least two replicate measurements were performed for each sample. Data processing was performed using OMNIC software (Thermo Fisher Scientific).[28]

The recorded spectra were compared with $Fe(OH)_3$ and FeOOH reference spectra obtained under identical conditions to facilitate phase identification. Peak assignments were based on characteristic vibrational modes: Fe-O stretching (400-700 cm-1), O-H bending (1600-1650 cm-1), O-H stretching (3000-3700 cm-1), and surface-adsorbed species.[25]

C. Synthesis of functionalized Fe_2O_3-NPs

Fe_2O_3-NPs were functionalized with three silane coupling agents (SiCA): propyltrimethoxysilane (PTMS, C3), octyltriethoxysilane (OTES, C8), and hexadecyltrimethoxysilane (HDTMS, C16).

Determination of Silane Coupling Agent (SiCA) Loading

To modulate surface hydrophobicity, three silane coupling agents with varying hydrocarbon chain lengths (propyltrimethoxysilane (PTMS), octyltriethoxysilane (OTES), and hexadecyltrimethoxysilane (HDTMS)) were employed. The coupling mechanism involves four stages: (i) hydrolysis of methoxy and ethoxy groups, (ii) condensation reactions, (iii)

hydrogen bonding with the substrate, and (iv) covalent bond formation with surface hydroxyl groups.

To preserve active sites on the nanoparticle surface, functionalization was restricted to less than 40% of the available surface area, thereby preventing surface saturation, minimizing silane multilayer formation, and avoiding additional intermolecular interactions that could hinder catalytic performance.

The theoretical mass of SiCA required per gram of nanoparticles was calculated using a spherical particle model based on monolayer coverage assumptions. The model incorporates the specific surface area of the nanoparticles determined by BET analysis, the effective cross-sectional area occupied by the silane molecule on the surface (*C-S AREA*), the desired fractional surface coverage (*Xfunc* < 0.4), and the mass of nanoparticles (*g NPs*). The calculation accounts for the steric hindrance of methoxy groups in the silane structure, which significantly influences the molecular footprint and limits packing density due to repulsive interactions between adjacent molecules. The required mass of SiCA *(g SiCA)* was determined using the following proposed relationship:

$$\frac{g\ SiCa}{g\ N_{PS}} = \frac{BET\ \left(\frac{m^2}{g\ N_{ps}}\right) * X_{fune} * MW_{SiCa}\left(\frac{g\ sica}{mol_{SiCa}}\right)}{C{-}S\ AREA\left(\frac{m^2}{molec}\right) * NA\quad \left(\frac{molec}{mol_{SiCa}}\right)} \quad (1)$$

where MW_{SiCA} is the molecular weight of the silane coupling agent and *NA* is Avogadro's number (6.022×10^{23} mol^{-1}). The effective cross-sectional area *C-S AREA* was estimated from the full molecular geometry including methoxy substituents using molecular dynamics with a CHARMM parameterization-based force field, which accounts for bond forces, angles, internal rotation, and Van del Walls non-bonding interactions.

For surface functionalization, 0.2 g of Fe_2O_3-NPs (~97% solid content) were dispersed in ethanol (95%, 20 mL) in a 50 mL Erlenmeyer flask. The suspension was stirred magnetically at 400 rpm for 20 min at room temperature to ensure complete particle deagglomeration and formation of a homogeneous dispersion.

The required amount of SiCA, calculated from the model above for the target surface coverage, was added dropwise to the particle dispersion under continuous stirring. Based on the theoretical calculations described equation 1 and using a molecular weight of 164.3 g/mol for propyltriethoxysilane (PTES, 97% purity), the required amount of silane coupling agent (30 µL, corresponding to ~28.5 mg of pure PTES) was added dropwise to the particle dispersion under continuous stirring. The reaction mixture was maintained under magnetic stirring at 400 rpm for 1 h at room temperature (25 ± 2°C) to allow hydrolysis of the ethoxy groups and subsequent condensation with surface hydroxyl groups on the nanoparticles.

After functionalization process, the Fe_2O_3-NPs modified were recovered by centrifugation (4000 rpm, 5 min) and the supernatant was carefully decanted. The particles were washed three times with ethanol (95%, 15 mL each) to remove unreacted silane and hydrolysis byproducts, with centrifugation (4000 rpm, 5 min) performed after each washing step. The washed nanoparticles were transferred to a ceramic crucible and dried on a hotplate (Thermo Scientific Cimarec+, USA) at 110°C for 10 min to remove residual ethanol and promote complete silane condensation on the surface.

The above procedure was repeated for coupling agents (PTMS, OTES, HDTMS) at the corresponding calculated loading for 20% surface coverage. For the systematic coverage study with HDTMS (5–40% surface coverage), the SiCA amount was scaled proportionally according to the model equation, keeping all other conditions constant.

D. Physicochemical Properties of the Functionalized Fe_2O_3-NPs

Contact angle measurements

The wettability of Fe_2O_3-NPs, both pristine and functionalized, was measured by dispersing 10 µl of a nanoparticle mixture in alcohol onto a glass sample holder. Hydrophilic or hydrophobic behavior was characterized by measuring the contact angle between the material surface and a water droplet using the sessile drop method. The measurements were performed using the ADVANCE software on a DSA24E droplet size analyzer (KRÜSS) with the Young-Laplace model fitted.

Surface chemical state

The chemical composition and oxidation states of surface elements were determined by X-ray photoelectron spectroscopy (XPS) using a SPECS surface analysis system equipped with a PHOIBOS 150 hemispherical analyzer, a 2D-CMOS detector, and a monochromatic Al Kα X-ray source (1486.6 eV) operated at 12 kV and 200 W. Measurements were performed under ultrahigh vacuum conditions (~1×10^{-7} Pa) at the Laboratorio Central de Ciencia de Superficies (SurfLab-UIS).[29]

Fe_2O_3 and functionalized Fe_2O_3-NP powder samples were mounted on stainless steel sample holders using conductive Cu tape and introduced into the analysis chamber via a load-lock system. Surface charging was compensated using a flood gun (FG 15/40-PS) operated at 94 µA and 3.6 eV. Survey spectra were acquired at 100 eV pass energy, while high-resolution

spectra for Fe 2p, Si 2p, O 1s, and C 1s regions were recorded at 20 eV pass energy to maximize energy resolution.

Data processing was performed using CasaXPS software (Casa Software Ltd).[30]

Stability of Fe2O3-NPs in Liquid Phase

The colloidal stability of the nanoparticles — defined as their resistance to sedimentation — was evaluated in polar and nonpolar media to select the appropriate formulation for Pickering emulsion preparation. Nanofluids were prepared by dispersing pristine and functionalized nanoparticles of varying surface hydrophobicity (contact angles 26°–167°) in water and a heptane/toluene mixture (75/25 v/v) at a concentration of 500 ppm, using ultrasonication for 5 min. Particle sedimentation was monitored by UV-Vis spectrophotometry (Thermo Scientific Evolution 201) at a wavelength of 400 nm as a function of time (up to 116 h in water and up to 4 h in the hydrocarbon mixture). All measurements were performed in triplicate.

Emulsion Formulation

Pickering emulsion was prepared by dispersing solid particles with different hydrophobicity using water/hydrocarbon mixtures. Nanofluids in polar (water) and nonpolar (heptane/toluene 75/25 v/v) solvents were first prepared as described above. The maximum particle concentration (0–2730 ppm) for stable emulsion formation was determined by progressive addition of nanoparticles to the two-phase liquid system. Emulsification was achieved by ultrasonication (Branson Sonifier 450, 5 min, 40% amplitude) of the water/hydrocarbon mixture (1:1 v/v). Two types of emulsions were formulated: oil-in-water (O/W) using hydrophilic particles (contact angle < 90°) and water-in-oil (W/O) using hydrophobic particles (contact angle > 90°), in accordance with the extended Bancroft rule for solid particle stabilizers.[19]

Catalytic performance of Pickering Emulsion

Catalytic tests were performed using emulsions stabilized with functionalized Fe_2O_3-NPs, following established Fenton-type reaction protocols.[31], [32] Fig. 1 depicts the reaction pathway for the catalytic oxidation of benzyl alcohol (BA) to benzoic acid via the intermediate benzaldehyde.

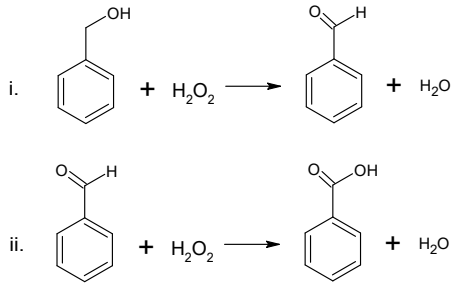


Fig.1. Sequential oxidation of benzyl alcohol to benzaldehyde and subsequent conversion to benzoic acid.

The following procedure was used: a defined amount of benzyl alcohol (n = 6.1 mmol, 0.63 mL) was added to the emulsion (5 mL total volume, 1:1 v/v water/heptane–toluene) dispersed in 2.5 mL of the non-polar phase at room temperature. The mixture was stirred at 500 rpm until a stable emulsion was formed (~5 min). Next, the temperature was raised to 50 °C using a thermostatically controlled water bath. Once the reaction temperature was reached, H_2O_2 (30% aqueous solution) was introduced as the oxidizing agent while maintaining a H_2O_2/Benzyl alcohol molar ratio of 6:1. The reaction mixture was then allowed to stand without stirring for 2 h. Fe_2O_3-NP loading was fixed at 2730 ppm relative to the total liquid volume based on emulsion stability results, and all experiments were performed in duplicate.

Aliquots (0.2 mL) were withdrawn from the organic and aqueous phases at fixed time intervals (0, 30, 60, 120, 250, 400, 600, and 780 min), diluted 10-fold with ethanol, and immediately analyzed by GC. Benzyl alcohol and benzaldehyde concentrations were measured using an HP 6890 gas chromatograph equipped with a flame ionization detector (FID) and a DB-WAX column (30 m × 0.25 mm × 0.25 µm film thickness), and biphenyl was used as internal standard.

III. RESULTS AND DISCUSSION

Synthesis and Characterization of Fe_2O_3*-NPs*

Fe_2O_3-NPs were synthesized via alkaline coprecipitation using the neutralization reaction between iron chloride dissolved in ethanol or acetone and sodium carbonate at low temperature and atmospheric pressure.[5], [6] The reaction can be described by Equation 2:

$$2FeCl_3 + 3Na_2CO_3 \xrightarrow[CH_3OCH_3]{} Fe_2O_3 + 6NaCl + 9CO_2 \quad (2)$$

Particle Size Analysis by DLS

Fig. 2 displays the light scattering patterns of Fe2O3 particles synthesized at varying $FeCl_3$ concentrations. A clear relationship between particle size and $FeCl_3$ concentration was

observed, with higher concentrations leading to larger particles, consistent with classical nucleation theory.[33] Fig. 2(b) illustrates the linear relationship between $FeCl_3$ precursor concentration and final particle size in Fe_2O_3-NPs synthesis, demonstrating the ability to control particle dimensions through precursor concentration.

At higher temperatures, sintering processes occur that lead to particle coalescence and size increase consistent with the progressive size evolution observed from 14.9 ± 0.1 nm (11 ppm $FeCl_3$) to 133 ± 4 nm (340 ppm $FeCl_3$) shown in the size distribution histograms.

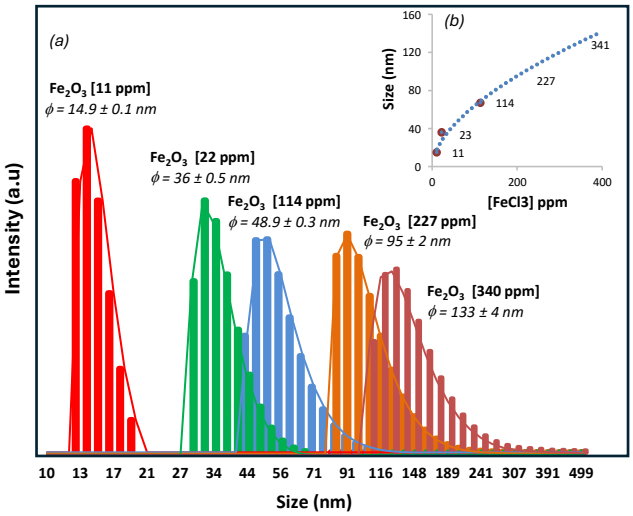


Fig. 2. Effect of $FeCl_3$ precursor concentration on the hydrodynamic diameter of Fe_2O_3-NPs. (a) Particle size distributions measured by DLS for selected $FeCl_3$ concentrations; (b) linear relationship between $FeCl_3$ concentration and mean particle diameter

X-ray Diffraction and TEM Analysis

XRD patterns of Fe_2O_3-NPs synthesized from 0.08% and 2% $FeCl_3$ solutions (Fig. 3) exhibit broad and low-intensity reflections, indicative of limited long-range crystallographic order, low peak resolution due to the small crystallite size, as crystalline growth typically requires temperatures above 300°C and extended crystallization times.[34],[25]

The broad, low-intensity peaks are characteristic of small crystalline materials rather than well-crystallized phases, consistent with the Scherrer equation for crystallite size determination.[35] The most intense peaks observed in the XRD patterns correspond to the (110) crystallographic plane of α-hematite as the dominant reflection.[25] This behavior is typically associated with nanometric crystallite size (< ~20 nm), lattice strain, and the presence of an amorphous fraction. Although dynamic light scattering (DLS) indicates hydrodynamic diameters of 27 nm and 95 nm, these values correspond to agglomerates rather than individual crystallites.

Despite the poor peak resolution, quantitative analysis of the diffraction pattern suggests a crystallinity degree of 74.85%, indicating that a significant fraction of the material is structurally ordered at the short range. According to the Scherrer-based approaches and their modern refinements, peak broadening increases inversely with crystallite size, although it is also affected by strain and defects. [35], [36], [37], [38]

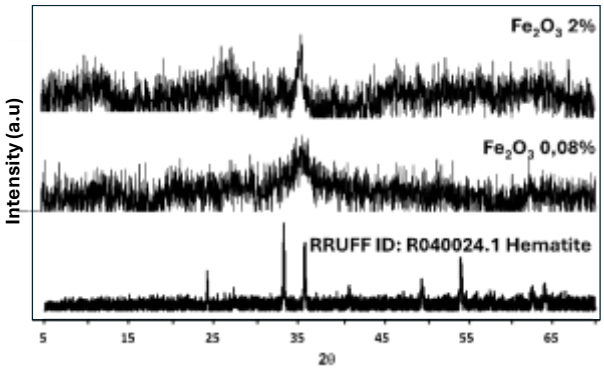


Fig. 3. X-ray diffraction patterns of Fe_2O_3-NPs synthesized from 0.08% and 2% $FeCl_3$ solutions, yielding particles of 27 nm and 95 nm (DLS), respectively. Reference peaks for α-hematite (JCPDS 33-0664) are indicated.

Fig.4a shows TEM micrographs of Fe_2O_3-NPs. The formation of hexagonal Fe_2O_3 crystal structures is highlighted in Fig. 4(b) showcase by the red lines. Hexagonal morphology of the Fe_2O_3-NPs is consistent with the particle sizes distribution measured by TEM in Fig. 4c and the XRD results. TEM micrograph shows well-resolved lattice fringes with d-spacings of 3.5 Å and 2.5 Å, corresponding to the (012) and (110) crystallographic planes of the hexagonal crystal system of α-hematite, respectively, see in Fig. 4b.[39], [40] These interplanar distances are consistent with the reported lattice parameters for hematite (a = 5.038 Å, c = 13.772 Å) and confirm the formation of the hematite phase under the employed synthesis conditions. TEM results provide complementary structural insight.

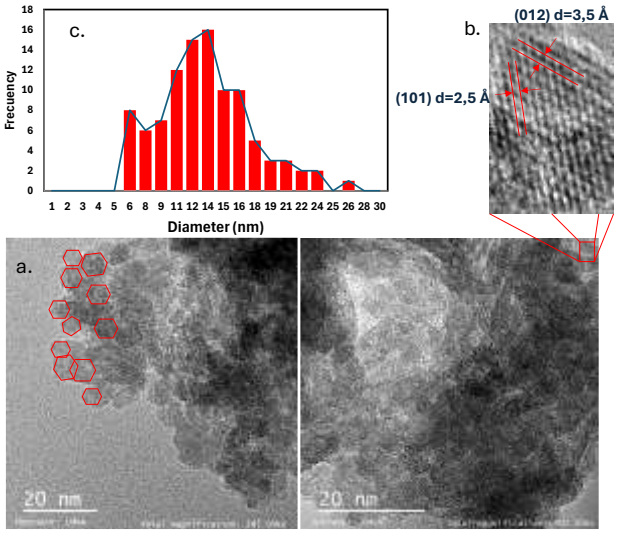


Fig. 4. Transmission electron microscopy analysis of Fe_2O_3-NPs. (a) Overview showing particle morphology and aggregation; (b) high-resolution micrograph revealing hexagonal crystal structure and lattice fringes with d-spacings of 3.5 Å (012) and 2.5 Å (110) consistent with α-hematite; (c) particle size distribution histogram from TEM analysis.

TEM micrographs reveal aggregates composed of quasi-hexagonal nanoparticles with an average size of ~12 nm, significantly smaller than the observed DLS values. This evidence shows that the larger sizes measured by DLS arise from particle agglomeration in suspension rather than primary particle size.[36], [41], [42]

XRD and TEM results indicate that the material consists of nanocrystalline domains embedded within partially disordered aggregates. The absence of sharp diffraction peaks is therefore not due to insufficient packing, but rather to the small crystallite size, lattice strain, and partial amorphous character, which limit long-range periodicity and reduce coherent diffraction. [36], [42]

FTIR-ATR Spectroscopic Analysis

FTIR-ATR spectra of synthesized Fe_2O_3-NPs were compared with reference spectra of iron hydroxide ($Fe(OH)_3$) and iron oxyhydroxide (FeOOH) as indicated in Fig. 5. Three distinct infrared absorption regions were identified: (i) the OH stretching region (2500–3700 cm-1) corresponding to hydrogen–oxygen bond stretching vibrations; the reduced intensity of OH groups indicates successful dehydration during the calcination process; (ii) the Fe–OH bending region (700–1700 v) characteristic of iron–hydroxyl interactions; and (iii) the Fe–O bending region (400–700 cm-1) corresponding to iron–oxygen bending vibrations typical of the Fe_2O_3 structure.[25] The spectrum confirms the formation of the Fe_2O_3 phase with minimal hydroxyl content, consistent with the synthesis and thermal treatment conditions employed.

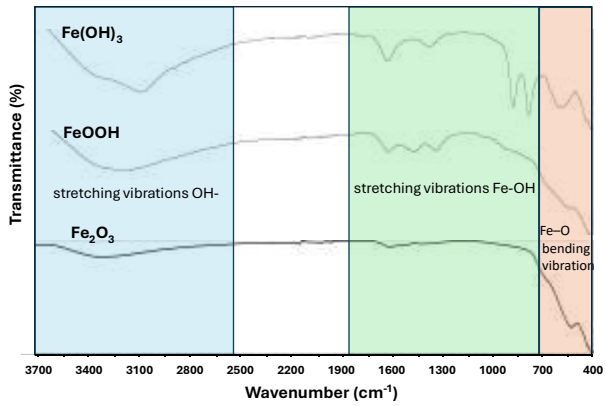


Fig. 5. FTIR-ATR spectra of synthesized Fe_2O_3-NPs compared with reference iron hydroxide ($Fe(OH)_3$) and iron oxyhydroxide (FeOOH). Key absorption regions are indicated: Fe–O bending (400–700 cm-1), Fe–OH bending (700–1700 cm-1), and O–H stretching (2500–3700 cm-1).

BET Surface Area Analysis

BET analysis revealed significant differences between the two synthesized Fe_2O_3-NPs samples. Particles with 27 nm diameter (DLS) exhibited a BET surface area of 114.7 m2/g (Fig. 6a), whereas 95 nm particles showed 62.5 m2/g (Fig. 6b), following the expected inverse relationship between particle size and specific surface area according to geometric principles.[28], [43]

The N_2 adsorption isotherms are classified as Type IV according to IUPAC classification, characteristic of multilayer adsorption on mesoporous materials. The BJH method revealed large average pore sizes, and considering the particle dimensions, the observed hysteresis likely corresponds to particle aggregation effects rather than intrinsic porosity.

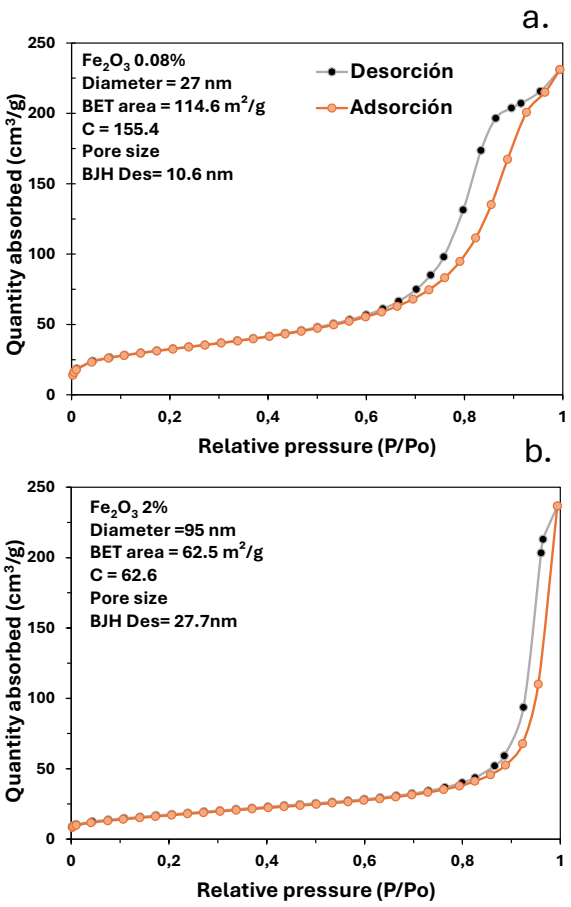


Fig. 6. N2 adsorption–desorption isotherms (77 K) of Fe_2O_3-NPs with mean hydrodynamic diameters of (a) 27 nm (BET = 114.7 m2/g) and (b) 95 nm (BET = 62.5 m2/g). Isotherms are classified as Type IV (IUPAC), indicating mesoporous character.

Surface Functionalization with Silane Coupling Agents

Table I presents molecular parameters and contact angles of Fe_2O_3-NPs functionalized at 20% surface coverage. Among the three candidates, HDTMS (C16) demonstrated the most pronounced hydrophobic behavior (126.7°). In addition, HDTMS presents superior effectiveness for the surface

modulation, and was selected for systematic hydrophilicity modulation studies.

TABLE I.
MOLECULAR PARAMETERS AND CONTACT ANGLES OF Fe_2O_3-NPs (95 nm, BET = 62.5 m^2/g)

SiCA	Molecule length (Å)	Face SiFA (m^2/molecule)	SiCA MW (g/mol)	% Area	mg SiCA/g	Contact Angle
Si (C 16)	21,23	3,7 E-19	346,6	20	360	126,7
Si (C 8)	11,14	3,7 E-19	234,4	20	244	75,6
Si (C 3)	8,17	3,7 E-19	164,3	20	171	35,4

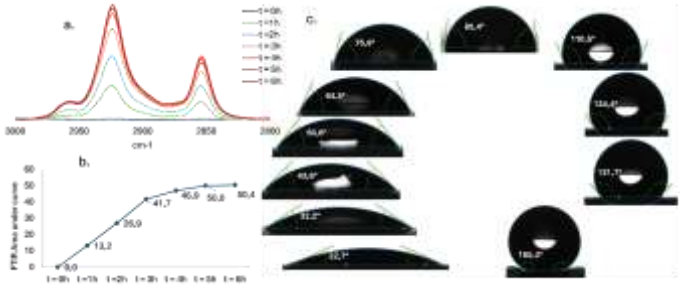


Fig. 7. Surface functionalization of Fe_2O_3-NPs with HDTMS. (a) DRIFT spectra in the C–H stretching region (2800–3000 cm-1) as a function of reaction time; (b) kinetics of HDTMS grafting monitored by the integrated C–H band intensity; (c) water contact angle as a function of HDTMS surface coverage (5–40%)

To achieve a broader range of surface wettabilities, the HDTMS loading was systematically varied from 5% to 40% surface coverage. This approach enabled fine-tuning of contact angles from 20° (pristine Fe_2O_3) to 167° (superhydrophobic), as shown in Fig. 7. The functionalization was deliberately restricted to a maximum of 40% coverage to prevent multilayer formation and preserve sufficient exposed Fe_2O_3active sites for catalytic applications. Higher coverage values (>40%) would risk complete surface passivation and loss of catalytic activity.

Fig. 7a shows the evolution of C-H stretching bands (2800-3000 cm-1) over time, demonstrating successful organic chain attachment. The functionalization kinetics (Fig. 7b) and resulting contact angle modulation (Fig. 7c) confirm the ability to precisely control surface hydrophilicity by varying the SiCA concentration while maintaining surface coverage below 40%, thereby preserving active sites for catalytic activity.

Surface Area Effects of Functionalization.

BET analysis of 95 nm HDTMS-functionalized Fe_2O_3-NPs with contact angles >90° revealed a 52.6% increase in surface area for 95 nm particles and a 14.0% increase for 27 nm particles compared to their respective pristine counterparts (Fig. 8). This increase is attributed to the disruption of nanoparticle aggregates caused by surface hydrophobization: the organic chains introduce steric repulsion between neighboring particles, reducing the interparticle contact area and exposing previously inaccessible surface regions.[23], [22], [23] Additionally, reduced hysteresis in the adsorption-desorption isotherms was observed, indicating decreased particle aggregation due to surface hydrophobic repulsion, which maintains total surface availability for N_2 adsorption.

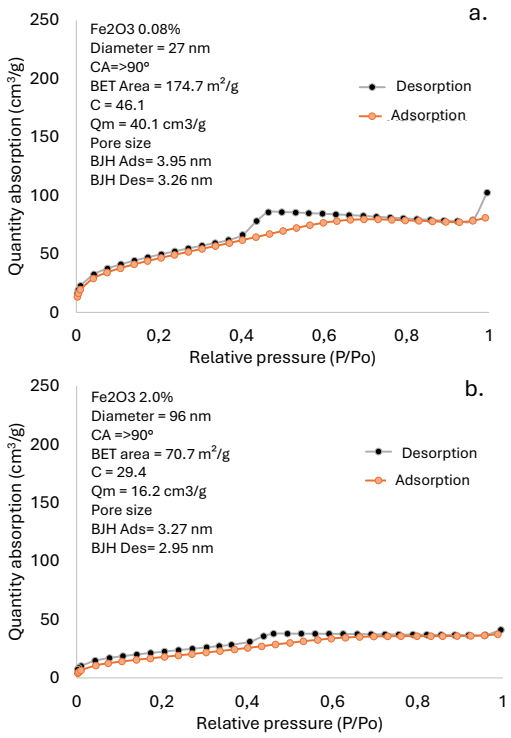


Fig. 8. BET specific surface area of pristine and HDTMS-functionalized Fe_2O_3-NPs (27 nm and 95 nm) as a function of contact angle. N2 adsorption–desorption isotherms are shown for samples with contact angle > 90° (hydrophobic regime)

XPS Surface Analysis.

X-ray photoelectron spectroscopy confirmed successful surface modification. The peaks associated with Fe 2p1/2 and 2p3/2 photoelectrons appeared at 724 eV and 710 eV, respectively, remaining unchanged upon functionalization (Fig. 9), consistent with literature values for bulk Fe_2O_3.[44]

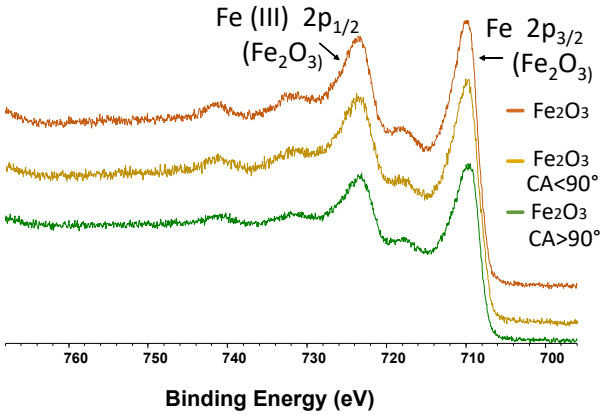


Fig. 9. High-resolution XPS spectra in the Fe 2p region for pristine and HDTMS-functionalized Fe2O3-NPs. Binding energies at 710 eV (Fe 2p3/2) and 724 eV (Fe 2p1/2) are consistent with Fe^{3+} in Fe2O3 and remain unchanged upon functionalization.

Silicon presence was detected through Si 2s electrons at 149 eV (Fig. 10) and Si 2p electrons at 99 eV, with peak intensity correlating with functionalization degree.

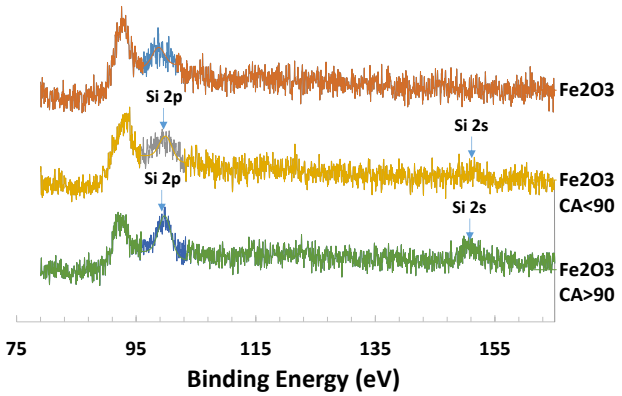


Fig. 10. High-resolution XPS spectra in the Si 2p and Si 2s regions for Fe_2O_3-NPs at increasing HDTMS surface coverages (0–40%), showing progressive increase in Si signal intensity with functionalization degree.

Oxygen 1s analysis revealed multiple oxygen environments on the particle surface (Fig. 11). Deconvolution showed decreased hydroxyl group concentration upon organic chain attachment and increased silicon content, confirming successful surface modification while maintaining the Fe2O3 core structure.

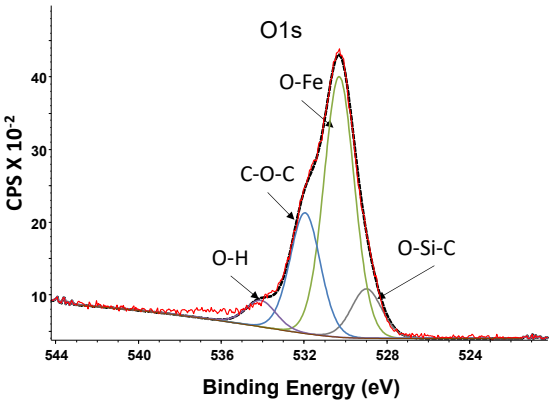


Fig. 11. High-resolution XPS spectra in the O 1s region for pristine and HDTMS-functionalized Fe_2O_3-NPs.

Deconvolution reveals contributions from lattice O (Fe–O), surface hydroxyl groups (Fe–OH), and siloxane/silanol groups (Si–O), with decreasing hydroxyl content upon functionalization.

Three main peaks are observed in the C1s region: one at 284 eV (C-C, C-H), another at 285.2 eV (C-O, C-Si), and a third at 289 eV (O-C=W) in Fig. 12. The relative intensity of these peaks increases from Fig. 12a (unfunctionalized) to Fig. 12c (CA>90°), confirming the progressive increase in surface organic coverage. The Si 2p/C 1s atomic ratio further supports this trend, with the sample Fe_2O_3 CA > 90° presenting the highest proportion of silicon, consistent with a higher degree of silane coating.

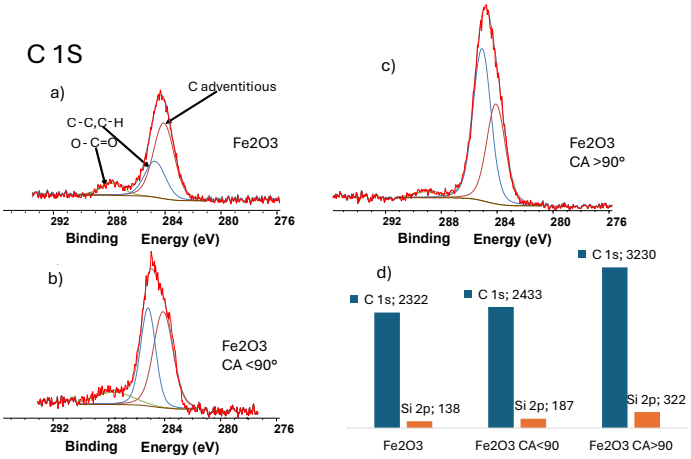


Fig. 12. High-resolution XPS spectra in the C 1s region for (a) pristine Fe_2O_3-NPs, (b) partially functionalized Fe_2O_3-NPs (CA < 90°), and (c) hydrophobic Fe_2O_3-NPs (CA > 90°). Peaks at 284.0 eV (C–C/C–H), 285.2 eV (C–O/C–Si), and 289.0 eV (C=O) increase in intensity with functionalization degree. Inset: Si 2p/C 1s atomic ratio as a function of surface coverage.

Nanofluid Stability in Different Liquid Phases

The Stability of Fe_2O_3-NPs in Aqueous Phase

Fe_2O_3-NPs stability in water was evaluated over 116 h Fig. 13. Non-Functionalized particles (contact angle 26°) exhibited excellent stability due to high surface hydroxyl concentration and the resulting electrostatic repulsion (zeta potential –35 mV), consistent with DLVO theory predictions.[45] [46] This high negative surface charge arises from deprotonated Fe–OH groups, which stabilize the colloidal system by increasing the energy barrier against aggregation.[47]

As the functionalization degree increased, aqueous dispersion stability decreased due to reduced surface OH groups density and lower zeta potential. This reduction weakens electrostatic repulsion and favors particle aggregation and sedimentation, as widely reported for partially hydrophobized oxide nanoparticles.[48], [49] Consequently, approximately 50% particle settling was observed after 116 h for functionalized samples.

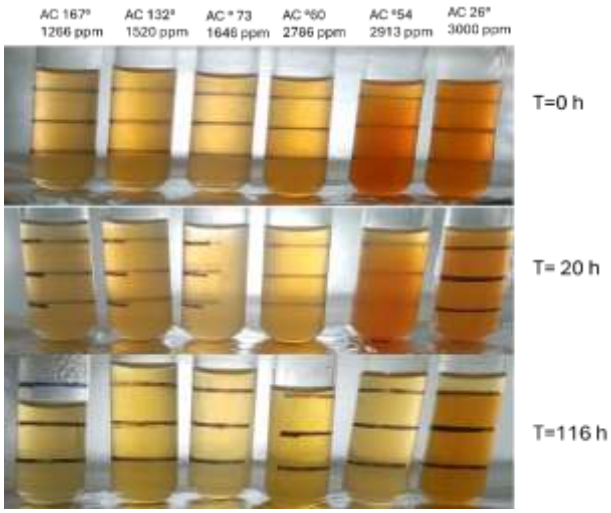


Fig.13. Colloidal stability of Fe_2O_3-NPs with varying HDTMS surface coverage in aqueous phase, monitored by UV-Vis absorbance (λ = 400 nm) over 116 h. Particle concentration is expressed relative to the initial value at t = 0.

These results confirm that the 20-40% coverage window represents an optimal balance: sufficient functionalization to enable interfacial activity at oil-water interfaces (essential for Pickering emulsion formation), yet moderate enough to prevent complete surface passivation and loss of catalytic sites.

The distribution of functionalized Fe_2O_3-NPs was measured based on the dispersion in each phase, as well as the formation and subsequent breakage of the emulsion, revealing that the particles are preferentially located at the interface Fig. 14.



Fig. 2. Preferential accumulation of HDTMS-functionalized Fe_2O_3-NPs at the water/hydrocarbon interface.

Images show the particle distribution in each phase after emulsification and subsequent phase separation.

Emulsion Types and Stability

Stable macro-emulsions were successfully formulated using particles with both hydrophilic (contact angle <90°) and lipophilic (contact angle >90°) surfaces (Fig. 15). This behavior is consistent with the extended Bancroft rule for solid particle stabilizers: particles with contact angle < 90° (preferential wetting by water) preferentially curve toward the oil phase, stabilizing oil-in-water (O/W) emulsions, while particles with contact angle > 90° (preferential wetting by oil) stabilize water-in-oil (W/O) emulsions.[19] A W/O macro-emulsion was stabilized by hydrophilic Fe_2O_3-NPs (Fig. 15a), and a O/W macro-emulsion stabilized by lipophilic Fe_2O_3-NPs Fig. 15b. The distribution and size of droplets of the emulsion are shown in Fig. 15c, showcasing the versatility of the functionalization approach for emulsion type control.

The droplet size distribution shows a bimodal profile. The number-based curve is dominated by small droplets (~5–20 µm), indicating efficient droplet breakup and stabilization by nanoparticle adsorption at the interface.[50], [51].

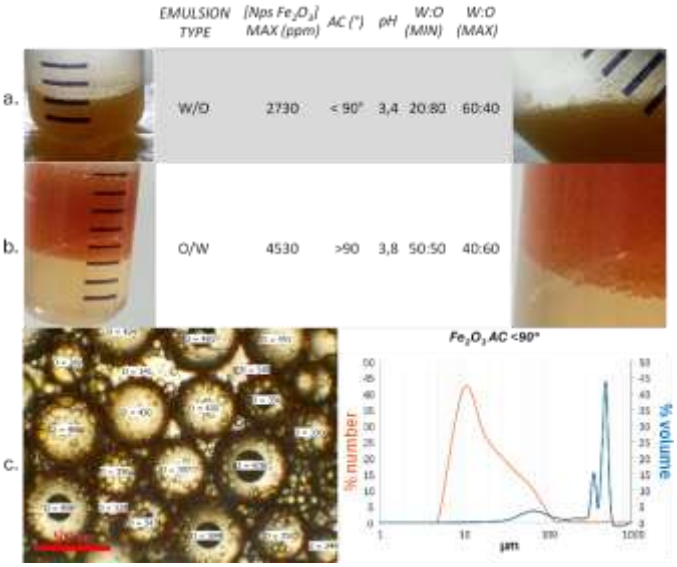


Fig. 3. Pickering emulsions stabilized by Fe_2O_3-NPs with different surface wettability. (a) W/O macro-emulsion stabilized by hydrophilic NPs (CA < 90°); (b) O/W macro-emulsion stabilized by hydrophobic NPs (CA > 90°); (c) optical microscopy images showing droplet size and distribution for each emulsion type

In the present work, the broader contact angle range achieved (20°–167°) through HDTMS loading variation allows access to both types of emulsions (O/W and W/O), offering additional design flexibility for catalytic applications.

Catalytic Reactivity of Fe_2O_3 Nanoparticles in Emulsion Media

The catalytic activity of Fe_2O_3-NPs with varying surface hydrophobicity was evaluated at 50°C using H_2O_2 as oxidizing agent, and three different contact angles from functionalization. Table. II summarizes the catalytic performance of Fe_2O_3 nanoparticles with different surface wettabilities during the oxidation of benzyl alcohol in Pickering emulsion systems.

TABLE II.
CATALYTIC PERFORMANCE OF Fe_2O_3-NPS WITH DIFFERENT SURFACE HYDROPHOBICITIES

Sample	Temperature (°C)	Time (min)	Contact Angle (°)	Conversion (%)
Particle-free system	50	780	N/A	13.3 ± 3.4
Fe-pristine	50	780	26	82.6 ± 3.5
Fe-54	50	780	54	85.1 ± 5.5
Fe-167	50	780	167	81.6 ± 7.5
Fe-54 H2O	50	780	54	86.1 ± 4.0
Particle-free system	50	900	N/A	15.9 ± 0.5
Fe-pristine	50	900	26	88.8 ± 0.1
Fe-54	50	900	54	88.6 ± 0.2
Fe-167	50	900	167	88.3 ± 0.1
Particle-free system	50	900	N/A	15.2
Fe-pristine H2O	50	900	26	88.9
Fe-54 H2O	50	900	54	88.9
Fe-167 H2O	50	900	167	88.4

Fe_2O_3-NPs with contact angles of 26° (Fe-pristine), 54° (Fe-54), and 167° (Fe-167) exhibited comparable catalytic performance, reaching benzyl alcohol conversions between approximately 83% after 780 min and 88.5 % after 900 min of reaction (Fig. 16). In contrast, the particle-free system showed significantly lower conversion values (~13–15%), confirming the essential catalytic role of Fe_2O_3 nanoparticles in the interfacial Fenton-type oxidation process.

Despite the substantial differences in nanoparticle wettability, HDTMS functionalization did not significantly affect catalytic activity, indicating that surface modification mainly alters interfacial behavior without blocking the Fe^{3+} active sites responsible for oxidation.

The distribution of benzyl alcohol in both phases after reaction maintained thermodynamic equilibrium, with similar conversion percentages observed in the two phases for Fe-54 (Fig. 16). This behavior suggests that the reaction predominantly occurs at the liquid–liquid interface, while continuous mass transfer between phases ensures a sustained supply of reactants for interfacial oxidation. In Fenton-type systems, the distribution of H_2O_2 and organic substrates between phases establishes a dynamic equilibrium that maintains catalytic activity and enhances overall conversion.[52], [53], [54].

Moreover, the results obtained at 13 h and 15 h indicate that the reaction approaches a stabilization regime at prolonged reaction times. This behavior is likely associated with competitive oxidation pathways and the accumulation of intermediate and secondary products such as benzaldehyde, benzoic acid, and other oxygenated compounds, which may compete with benzyl alcohol for active radical species and catalytic sites.

The use of H_2O_2 as oxidant via the Fenton mechanism provides a complementary pathway to aerobic oxidation, particularly relevant when gaseous O_2 delivery is impractical. Furthermore, the ability of Fe_2O_3-NPs to simultaneously stabilize the emulsion and provide catalytic active sites—without requiring an additional noble metal loading step—represents a simplification in catalyst design.

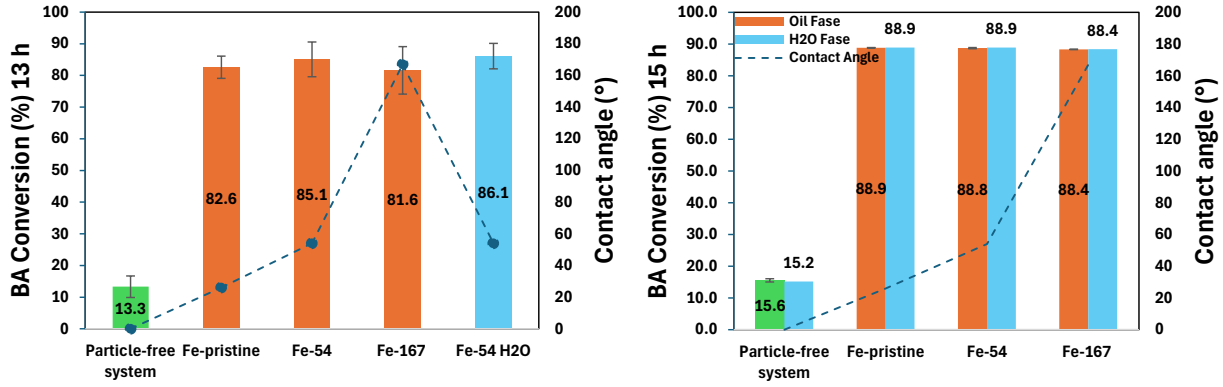


Fig. 4. Benzyl Alcohol Conversion in Oil and Aqueous Phases of Fe_2O_3-Stabilized Pickering Emulsions at Different Reaction Times.

The oxidation of benzyl alcohol followed zero-order kinetics in the initial phase (up to ~60% conversion), characteristic of surface-saturated catalytic processes Fig.17. The reaction proceeded through sequential oxidation: benzyl alcohol → benzaldehyde → benzoic acid, with concurrent aromatic ring opening to produce maleic acid, as evidenced by measurement in the phase.

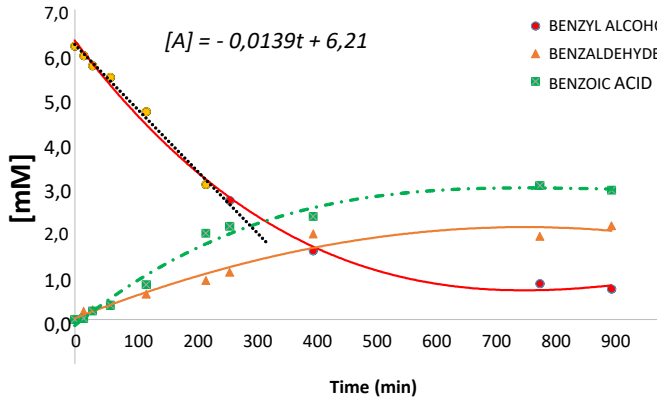


Fig. 5. Zero-order kinetic model for benzyl alcohol oxidation with H_2O_2 at 50°C over superhydrophobic Fe_2O_3-NPs (CA = 167°, 40% HDTMS coverage) in Pickering emulsion. The linear regime ([A] = −0.0139t + 6.21) is valid up to ~60% conversion; the kinetic transition at ~300 min indicates onset of consecutive oxidation reactions.

The kinetic behavior of benzyl alcohol oxidation at 50°C in the emulsion system stabilized by superhydrophobic Fe_2O_3-NPs (contact angle 167°) shows a linear decrease in benzyl alcohol concentration independent of reactant concentration, the reaction exhibits zero-order kinetics,[55] characterized by a linear decrease in benzyl alcohol concentration independent of reactant concentration, as described by the equation:

$$[A] = -0.0139t + 6.21 \qquad (3)$$

A significant kinetic transition occurs at approximately 300 min, where the linear relationship deviates, indicating a shift from zero-order to mixed-order kinetics.

The quantitative kinetic analysis using Fe_2O_3-NPs with 167° contact angle yielded a zero-order rate constant of $k_0 = 1.36 \times 10^{-4}$ mol·L^{-1}·min^{-1}, an activation energy of 104.1 kJ/mol, and a pre-exponential factor of 8.95×10^{11} mol·L^{-1}·min^{-1}. The activation energy value is comparable to the 103 k

J/mol reported by Wang et al. for Pd/non-JP particles under non-foaming conditions,[22] suggesting that in the present emulsion system the reaction predominantly occurs at the liquid–solid interface rather than at a gas–liquid–solid three-phase interface as in the oil foam systems. The proposed kinetic model accurately describes the reaction behavior up to 60% conversion, beyond which the consecutive reaction mechanism becomes predominant.

$$[BA]_t = [BA]_o - 8.95x10^{11}e^{-\frac{12521}{T}} * t \qquad (4)$$

Where [BA]t is the concentration of benzyl alcohol for a time t, [BA]o is the initial concentration of benzyl alcohol, and T the reaction temperature (K).

Beyond 60% conversion, the kinetics deviate from zero-order behavior due to competitive reactions involving benzaldehyde oxidation and product inhibition effects at the Fe2O3 surface.[56]

IV. Conclusion

This study demonstrates the controlled surface functionalization of Fe_2O_3-NPs using silane coupling agents of varying alkyl chain lengths (C3, C8, and C16) and their application as dual-function materials for Pickering emulsion stabilization and catalytic oxidation reactions.

HDTMS (C16) proved most effective for hydrophobic conversion, while PTMS (C3) provided moderate hydrophilicity modulation.

The functionalized Fe_2O_3-NPs exhibited versatile performance as Pickering emulsion stabilizers, with emulsion

CC BY NC SA

type (W/O or O/W) and stability directly correlated to the engineered hydrophilic–hydrophobic balance.

The Fe_2O_3-NPs demonstrated effective catalytic performance for benzyl alcohol oxidation in Pickering emulsion systems, achieving ~83% conversion at 50°C using H_2O_2 as oxidant. The zero-order kinetics (Ea = 104.1 kJ/mol) are consistent with surface-controlled catalysis at the oil–water interface, and the observed kinetic transition at ~60% conversion is attributed to competitive product inhibition by benzaldehyde.

ACKNOWLEDGMENT

The authors acknowledge the Doctoral Program in Chemistry, the School of Chemistry, the Research Center for Catalysis (CICAT), and the Surface Science Laboratory (SURFLAB) at Universidad Industrial de Santander.

REFERENCES

[1] A. K. Gupta and M. Gupta, "Synthesis and surface engineering of iron oxide nanoparticles for biomedical applications," *Biomaterials*, vol. 26, no. 18, pp. 3995–4021, 2005, https://doi.org/10.1016/j.biomaterials.2004.10.012.

[2] Y. Gandon, J.-F. Heautot, F. Brunet, D. Guyader, Y. Deugnier, and M. Carsin, "Superparamagnetic iron oxide: clinical time-response study," *Eur. J. Radiol.*, vol. 12, no. 3, pp. 195–200, 1991, https://doi.org/10.1016/0720-048X(91)90072-4.

[3] B. I. Kharisov, H. V Rasika Dias, O. V Kharissova, V. Manuel Jiménez-Pérez, B. Olvera Pérez, and B. Muñoz Flores, "Iron-containing nanomaterials: synthesis, properties, and environmental applications," *RSC Adv.*, vol. 2, no. 25, pp. 9325–9358, 2012, https://doi.org/10.1039/C2RA20812A

[4] [4] Cornell R. ; Schwertmann U., The Iron Oxides: Structure, Properties, Reactions, Occurences and Uses, 2nd ed. Wiley, 2003.

[5] [5] J.-P. Jolivet, E. Tronc, and C. Chanéac, "Iron oxides: From molecular clusters to solid. A nice example of chemical versatility," *Comptes Rendus Geoscience*, vol. 338, no. 6, pp. 488–497, 2006, https://doi.org/10.1016/j.crte.2006.04.014

[6] [6] R. Massart, "Preparation of aqueous magnetic liquids in alkaline and acidic media," *IEEE Trans. Magn.*, vol. 17, no. 2, pp. 1247–1248, 1981, https://doi.org/10.1109/TMAG.1981.1061188

[7] [7] L. H. Reddy, J. L. Arias, J. Nicolas, and P. Couvreur, "Magnetic Nanoparticles: Design and Characterization, Toxicity and Biocompatibility, Pharmaceutical and Biomedical Applications," *Chem. Rev.*, vol. 112, no. 11, pp. 5818–5878, Nov. 2012, https://doi.org/10.1021/cr300068p

[8] [8] W. Wu, Q. He, and C. Jiang, "Magnetic Iron Oxide Nanoparticles: Synthesis and Surface Functionalization Strategies," *Nanoscale Res. Lett.*, vol. 3, no. 11, pp. 397–415, 2008, https://doi.org/10.1007/s11671-008-9174-9

[9] [9] T. Ahmad, R. Phul, and H. Khan, "Iron oxide nanoparticles: An efficient nano-catalyst," *Curr. Org. Chem.*, vol. 23, no. 9, pp. 994 – 1004, 2019, https://doi.org/10.2174/1385272823666190314153208 .

[10] [10] M. Parthasarathy and C. N. Mohan, *Catalytic applications of iron oxide nanoparticles*. 2021. ISBN: 978-1-68507-006-9

[11] [11] I. T. Papadas, S. Fountoulaki, I. N. Lykakis, and G. S. Armatas, "Controllable Synthesis of Mesoporous Iron Oxide Nanoparticle Assemblies for Chemoselective Catalytic Reduction of Nitroarenes," *Chemistry - A European Journal*, vol. 22, no. 13, pp. 4600 – 4607, 2016, https://doi.org/10.1002/chem.201504685.

[12] [12] S. F. Hasany, N. H. Abdurahman, A. R. Sunarti, and R. Jose, "Magnetic iron oxide nanoparticles: Chemical synthesis and applications review," *Curr. Nanosci.*, vol. 9, no. 5, pp. 561 – 575, 2013, https://doi.org/10.2174/15734137113099990085.

[13] [13] S. Batool and Z. Hussain, "Diospyros lotus-mediated synthesis of iron oxide nanoparticles and their application as a catalyst in fenton reaction," *Curr. Nanosci.*, vol. 16, no. 1, pp. 91 – 100, 2020, https://doi.org/10.2174/1573413715666191023103729

[14] [14] G. Kickelbick, "Concepts for the incorporation of inorganic building blocks into organic polymers on a nanoscale," *Prog. Polym. Sci.*, vol. 28, no. 1, pp. 83–114, 2003, https://doi.org/10.1016/S0079-6700(02)00019-9.

[15] [15] C. Sanchez, B. Julián, P. Belleville, and M. Popall, "Applications of hybrid organic–inorganic nanocomposites," *J. Mater. Chem.*, vol. 15, no. 35–36, pp. 3559–3592, 2005, https://doi.org/10.1039/B509097K.

[16] [16] X. Huang *et al.*, "Magnetic nanoparticles with functional silanes: Evolution of well-defined shells from anhydride containing silane," *J. Mater. Chem.*, vol. 19, no. 24, pp. 4231–4239, 2009, https://doi.org/10.1039/b821917f.

[17] [17] P. Thissen *et al.*, "Activation of surface hydroxyl groups by modification of H-terminated Si(111) surfaces," *J. Am. Chem. Soc.*, vol. 134, no. 21, pp. 8869–8874, 2012, https://doi.org/10.1021/ja300270w.

[18] [18] X. Song and J.-F. Boily, "Water vapor interactions with FeOOH particle surfaces," *Chem. Phys. Lett.*, vol. 560, pp. 1–9, 2013, https://doi.org/10.1016/j.cplett.2012.12.048.

[19] [19] B. P. Binks and S. O. Lumsdon, "Influence of Particle Wettability on the Type and Stability of Surfactant-Free Emulsions†," *Langmuir*, vol. 16, no. 23, pp. 8622–8631, Nov. 2000, https://doi.org/10.1021/LA000189S.

[20] [20] B. P. Binks and A. T. Tyowua, "Oil-in-oil emulsions stabilised solely by solid particles," *Soft Matter*, vol. 12, no. 3, pp. 876–887, 2016, https://doi.org/10.1039/C5SM02438B.

[21] [21] B. P. Binks, "Colloidal Particles at a Range of Fluid–Fluid Interfaces," *Langmuir*, vol. 33, no. 28, pp. 6947–6963, Jul. 2017, https://doi.org/10.1021/ACS.LANGMUIR.7B00860.

[22] K. Wang, J. Davies-Jones, A. Graf, M. Carravetta, P. R. Davies, and M. Pera-Titus, "Amphiphilic Janus Particles for Aerobic Alcohol Oxidation in Oil Foams," *ACS Catal.*, vol. 14, no. 15, pp. 11545–11553, Aug. 2024, https://doi.org/10.1021/acscatal.4c00909.

[23] S. Zhang, D. Dedovets, A. Feng, K. Wang, and M. Pera-Titus, "Pickering Interfacial Catalysis for Aerobic Alcohol Oxidation in Oil Foams," *J. Am. Chem. Soc.*, vol. 144, no. 4, pp. 1729–1738, Feb. 2022, https://doi.org/10.1021/JACS.1C11207.

[24] R. Massart, "Preparation of aqueous magnetic liquids in alkaline and acidic media," *IEEE Trans. Magn.*, vol. 17, no. 2, pp. 1247–1248, 1981, https://doi.org/10.1109/TMAG.1981.1061188.

[25] R. M. Cornell and U. Schwertmann, "The Iron Oxides," *The Iron Oxides*, Jul. 2003, https://doi.org/10.1002/3527602097.

[26] V. G. Baldovino-Medrano, V. Niño-Celis, and R. Isaacs Giraldo, "Systematic Analysis of the Nitrogen Adsorption–Desorption Isotherms Recorded for a Series of Materials Based on Microporous–Mesoporous Amorphous Aluminosilicates Using Classical Methods," *J. Chem. Eng. Data*, vol. 68, no. 9, pp. 2512–2528, Sep. 2023, https://doi.org/10.1021/ACS.JCED.3C00257.

[27] A. A. Bunaciu, E. G. Udriştioiu, and H. Y. Aboul-Enein, "X-Ray Diffraction: Instrumentation and Applications," *Crit. Rev. Anal. Chem.*, vol. 45, no. 4, pp. 289–299, 2015, https://doi.org/10.1080/10408347.2014.949616.

[28] M. Thommes *et al.*, "Physisorption of gases, with special reference to the evaluation of surface area and pore size distribution (IUPAC Technical Report)," *Pure and Applied Chemistry*, vol. 87, no. 9–10, pp. 1051–1069, Oct. 2015, https://doi.org/10.1515/PAC-2014-1117.

[29] J. Rodríguez-Pereira, R. Valderrama-Zapata, L. J. Hoyos-Marín, and V. G. Baldovino-Medrano, "Surface Composition–Performance Relationships in Pt-Re/γ-Al_2O_3 for Catalytic Alkane Reforming and Aromatization," *ChemCatChem*, vol. 18, no. 1, p. e00569, Jan. 2026, https://doi.org/10.1002/CCTC.202500569

[30] P. Simon, V. G. Baldovino-Medrano, and R. Wojcieszak, "X-Ray Photoelectron Spectroscopy (XPS): Principles and Application for the Analysis of Photoactive Materials," *Springer Handbooks*, pp. 249–271, 2022, https://doi.org/10.1007/978-3-030-63713-2_10

[31] J. J. Pignatello, E. Oliveros, and A. MacKay, "Advanced Oxidation Processes for Organic Contaminant Destruction Based on the Fenton Reaction and Related Chemistry," *Crit. Rev.*

Environ. Sci. Technol., vol. 36, no. 1, pp. 1–84, Jan. 2006, https://doi.org/10.1080/10643380500326564.

[32] H. J. H. Fenton, "LXXIII.—Oxidation of tartaric acid in presence of iron," *Journal of the Chemical Society, Transactions*, vol. 65, no. 0, pp. 899–910, 1894, https://doi.org/10.1039/CT8946500899.

[33] [33] V. K. LaMer and R. H. Dinegar, "Theory, Production and Mechanism of Formation of Monodispersed Hydrosols," *J. Am. Chem. Soc.*, vol. 72, no. 11, pp. 4847–4854, Nov. 1950, https://doi.org/10.1021/ja01167a001.

[34] S. Menchaca-Nal, C. L. Londoño-Calderón, D. C. Pardo-Saavedra, L. G. Pampillo, L. M. Socolovsky, and R. Martínez-García, "Estudio del efecto del tamaño en la estructura cristalina de nanopartículas de CoFe2O4 study of the effect of the size in the crystalline structure of CoFe2O4 nanoparticles". An. AFA, vol. 25, no. 1, Aug. 2014, https://doi.org/10.31527/analesafa.2014.25.1.42.

[35] A. L. Patterson, "The Scherrer Formula for X-Ray Particle Size Determination," *Physical Review*, vol. 56, no. 10, p. 978, Nov. 1939, https://doi.org/10.1103/PhysRev.56.978.

[36] B. D. Cullity and S. R. Stock, "Elements of x-ray diffraction," p. 664, 2001.

[37] S. A. Hassanzadeh-Tabrizi, "Precise calculation of crystallite size of nanomaterials: A review," *J. Alloys Compd.*, vol. 968, p. 171914, Dec. 2023, https://doi.org/10.1016/J.JALLCOM.2023.171914.

[38] S. Nasiri *et al.*, "Modified Scherrer equation to calculate crystal size by XRD with high accuracy, examples Fe2O3, TiO2 and V2O5," *Nano Trends*, vol. 3, Sep. 2023, https://doi.org/10.1016/j.nwnano.2023.100015.

[39] C.-J. Jia *et al.*, "Large-Scale Synthesis of Single-Crystalline Iron Oxide Magnetic Nanorings," *J. Am. Chem. Soc.*, vol. 130, no. 50, pp. 16968–16977, Dec. 2008, https://doi.org/10.1021/ja805152t.

[40] E. J. W. Verwey, "The Crystal Structure of γ-Fe2O3 and γ-Al2O3," vol. 91, no. 1–6, pp. 65–69, 1935, https://doi.org/10.1524/zkri.1935.91.1.65.

[41] "X-ray diffraction : Warren, B. E. (Bertram Eugene), 1902- : Free Download, Borrow, and Streaming : Internet Archive." Accessed: Apr. 22, 2026. [Online]. Available: https://archive.org/details/xraydiffraction00warr

[42] H. P. Klug, L. E. Alexander, Klug, H. P., Alexander, and L. E., "X-Ray Diffraction Procedures: For Polycrystalline and Amorphous Materials, 2nd Edition," *xdpf*, p. 992, 1974, Accessed: Apr. 22, 2026. [Online]. Available: https://ui.adsabs.harvard.edu/abs/1974xdpf.book.....K/abstract

[43] F. Rouquerol, J. Rouquerol, and K. Sing, "Assessment of Surface Area," *Adsorption by Powders and Porous Solids*, pp. 165–189, Jan. 1999, https://doi.org/10.1016/B978-012598920-6/50007-5.

[44] X. Shi *et al.*, "NaCl-assisted synthesis of Fe2+ self-doped Fe2O3/C3N4 nanosheets as efficient Fenton catalyst," *J. Mater. Sci.*, vol. 55, no. 23, pp. 10035–10046, Aug. 2020, https://doi.org/10.1007/S10853-020-04775-4

[45] J. N. Israelachvili, "Intermolecular and Surface Forces, Academic Press, New York, 1992.," 2011, https://doi.org/10.1016/B978-0-12-375182-9.10020-X.

[46] Robert J. Hunter, "Zeta Potential in Colloid Science: Principles and Applications - Robert J. Hunter - Google Libros," *ISSN 0305-9723*, pp. 7–10, 1988, Accessed: Apr. 22, 2026. [Online]. Available: https://books.google.com.mx/books?hl=es&lr=&id=9I3-BAAAQBAJ&oi=fnd&pg=PP1&dq=zeta+potential+measurements+scientific+value&ots=EWY0P6PpUu&sig=hvtwbFx-7hXk7R9ADnXYenBM_3M#v=onepage&q&f=false

[47] M. Kosmulski, "Surface charging and points of zero charge," *Surface Charging and Points of Zero Charge*, pp. 1–1065, Jan. 2009, https://doi.org/10.1201/9781420051896.

[48] S. Bhattacharjee, "DLS and zeta potential – What they are and what they are not?," *Journal of Controlled Release*, vol. 235, pp. 337–351, Aug. 2016, https://doi.org/10.1016/J.JCONREL.2016.06.017.

[49] R. J. Hunter, "Electrified Interfaces: Ther Electrical Double Layer," *Foundations of Colloid Science*, pp. 304–337, 2001.

[50] R. Aveyard, B. P. Binks, and J. H. Clint, "Emulsions stabilised solely by colloidal particles," *Adv. Colloid Interface Sci.*, vol. 100–102, no. SUPPL., pp. 503–546, Feb. 2003, https://doi.org/10.1016/S0001-8686(02)00069-6.

[51] B. P. Binks and T. S. Horozov, "Colloidal Particles at Liquid Interfaces," *Colloidal Particles at Liquid Interfaces*, vol. 9780521848466, pp. 1–503, Jan. 2006, https://doi.org/10.1017/CBO9780511536670.

[52] B. P. Binks and J. A. Rodrigues, "Inversion of emulsions stabilized solely by ionizable nanoparticles," *Angew. Chem. Int. Ed.*, vol. 44, no. 3, pp. 441–444, Jan. 2005, https://doi.org/10.1002/ANIE.200461846

[53] M. Pera-Titus, V. García-Molina, M. A. Baños, J. Giménez, and S. Esplugas, "Degradation of chlorophenols by means of advanced oxidation processes: a general review," *Appl. Catal. B*, vol. 47, no. 4, pp. 219–256, Feb. 2004, https://doi.org/10.1016/J.APCATB.2003.09.010.

[54] E. Neyens and J. Baeyens, "A review of classic Fenton's peroxidation as an advanced oxidation technique," *J. Hazard. Mater.*, vol. 98, no. 1, pp. 33–50, 2003, https://doi.org/10.1016/S0304-3894(02)00282-0.

[55] L. K. Jang, R. L. York, and L. R. Hile, "A note on zero-order reactions in porous catalysts," *Journal of the Chinese Institute of Chemical Engineers*, vol. 34, no. 3, pp. 319–325, 2003.

[56] M. Sankar *et al.*, "The benzaldehyde oxidation paradox explained by the interception of peroxy radical by benzyl alcohol," *Nature Communications 2014 5:1*, vol. 5, no. 1, pp. 3332-, Feb. 2014, https://doi.org/10.1038/ncomms4332.



Fernando Martínez Ortega received the B.S. degree in chemistry and the M.S. degree in chemistry from the Universidad Industrial de Santander, Bucaramanga, Colombia, in 1989 and 1992, respectively, and the Ph.D. degree in chemistry from the Université de Poitiers, Poitiers, France, in 2000. He completed postdoctoral research in chemistry at the Université de Poitiers from 2010 to 2011. Since 1990, he has been with the School of Chemistry, Universidad Industrial de Santander, Bucaramanga, where he is currently a Full Professor. He is a member of the Catalysis Research Center (CICAT). His research interests include environmental catalysis, photocatalysis, selective oxidation by oxygen-atom transfer, catalyst heterogenization, oleochemistry, and the synthesis of metal nanoparticles. orcid.org/0000-0002-5931-4712



Wilson G. Oyola was born in Oiba, Santander, Colombia in 1977. He received the B.S. and M.S. degrees in Chemistry from the Industrial of Santander University, in 2006 and 2015. From 2008 to 2016, he was a Research Professional with the T.I.P Ltda. From 2017 to 2019, he was a Professor with the Basic Science Department, Santo Tomás University. He is the author of three inventions registered to Ecopetrol. His research interests include spectroscopic analytical, in Oil&Gas Upgrading of heavy crudes, synthesis of additives, heterogeneous catalysis, gold and silver purity processes, and chemical recycling of polymers in pyrolysis process in the ICPET Instituto

Colombiano del Petróleo y Energías de la Transición. orcid.org/0009-0000-8971-6248



Víctor Gabriel Baldovino Medrano Associate Professor at the School of Chemical Engineering at Universidad Industrial de Santander, Colombia. He completed undergraduate studies in Engineering (1998 – 2003) and a PhD in Chemical Engineering (2004 – 2009) at t Universidad Industrial de Santander. Subsequently, he was a postdoctoral researcher (2009 – 2014) at the Université catholique de Louvain (UC Louvain) in Belgium. He has taught courses on Applied Statistics and Design of Experiments, Transport Phenomena, Catalysis, and Surface Science. His research focuses on the synthesis and properties of materials and catalytic processes involving solids at various scales, with a particular emphasis on applications in hydrogenation and oxidation. His publication record is available on Google Scholar. He is the author of three patents and has published book chapters on Janus nanoparticles for catalytic applications and on the analysis of metal oxides using X-ray photoelectron emission spectroscopy. Recently, he published a book on Design of Experiments, featuring illustrative examples in catalysis. He has also served as a guest editor for journals such as Catalysis Today and ChemCatChem, and was the editor-in-chief of Revista ION. Currently, he is a member of the editorial committees of Molecular Catalysis and ChemCatChem. He has held leadership positions as Director of the Centro de Investigaciones en Catálisis (CICAT-UIS) and Scientific Coordinator of the Laboratorio Central de Ciencia de Superficies (SurfLab-UIS). Additionally, he served as President of the Colombian Society of Catalysis (2019–2023) and has been a member of the Ibero-American Federation of Catalysis Societies (FiSoCat) since 2019. He currently represents FiSoCat before the International Association of Catalysis Societies (IACS). orcid.org/0000-0003-3227-0251